15.34% efficiency all-small-molecule organic solar cells with an improved fill factor enabled by a fullerene additive

Hu, Dingqin; Yang, Qianguang; Chen, Haiyan; Wobben, Friso; Le Corre, Vincent M.; Singh, Ranbir; Liu, Tao; Ma, Ruijie; Tang, Hua; Koster, L. Jan Anton

Published in:
Energy & Environmental Science

DOI:
10.1039/d0ee00714e

Publication date:
2020

Energy & Environmental Science

ROYAL SOCIETY OF CHEMISTRY

PAPER

View Article Online
View Journal | View Issue

Cite this: *Energy Environ. Sci.*, 2020, **13**, 2134

15.34% efficiency all-small-molecule organic solar cells with an improved fill factor enabled by a fullerene additive†

Dingqin Hu,‡[a] Qianguang Yang,‡[a] Haiyan Chen,[a] Friso Wobben,[b] Vincent M. Le Corre,[b] Ranbir Singh,[c] Tao Liu,[d] Ruijie Ma,[d] Hua Tang,[a] L. Jan Anton Koster,[b] Tainan Duan,[a] He Yan,[d] Zhipeng Kan,*[a] Zeyun Xiao*[a] and Shirong Lu*[a]

Received 23rd January 2020,
Accepted 27th May 2020

DOI: 10.1039/d0ee00714e

rsc.li/ees

Solution processed organic solar cells (OSCs) composed of all small molecules (ASM) are promising for production on an industrial scale owing to the properties of small molecules, such as well-defined chemical structures, high purity of materials, and outstanding repeatability from batch to batch synthesis. Remarkably, ASM OSCs with power conversion efficiency (PCE) beyond 13% were achieved by structure improvement of the electron donor and choosing **Y6** as the electron acceptor. However, the fill factor (FF) is an obstacle that limits the further improvement of the PCE for these ASM OSCs. Herein, we focus on the FF improvement of recently reported ASM OSCs with **BTR-Cl**:**Y6** as the active layer by miscibility-induced active layer morphology optimization. The incorporation of fullerene derivatives, which have good miscibility with both **BTR-Cl** and **Y6**, results in reduced bimolecular recombination and thus improved FF. In particular, when *ca.* 5 wt% of $PC_{71}BM$ was added in the active layer, a FF of 77.11% was achieved without sacrificing the open circuit voltage (V_{OC}) and the short circuit current density (J_{SC}), leading to a record PCE of 15.34% (certified at 14.7%) for ASM OSCs. We found that the optimized device showed comparable charge extraction, longer charge carrier lifetime, and slower bimolecular recombination rate compared with those of the control devices (w/o fullerene). Our results demonstrate that the miscibility driven regulation of active layer morphology by incorporation of a fullerene derivative delicately optimizes the active layer microstructures and improves the device performance, which brings vibrancy to OSC research.

Broader context

Owing to the unique properties of small molecules, like their well-defined chemical structures, high purity of materials, and outstanding repeatability from batch to batch synthesis, ASM OSCs are promising for productions on an industrial scale. With efforts in donor material design, a power conversion efficiency (PCE) beyond 13% was reported for ASM OSCs with **Y6** as the electron acceptor. However, the fill factor (FF) of such solar cells is still lower than that of their polymer counterparts. FF is strongly affected by the active layer morphology and determined by the competition between the extraction and recombination of free charges. Thus, to further improve the FF, morphology optimization and charge carrier dynamics must be considered. On the other hand, the regulation of miscibility-induced microstructures has potential to improve the charge extraction and reduce the bimolecular recombination, which assists the FF enhancement. Therefore, it is critical to understand how the miscibility driven active layer morphology optimizations influence the charge carrier dynamics and the FF. To this end, we selected ASM OSCs composed of **BTR-Cl**:**Y6** to illustrate how incorporating more miscible materials, such as fullerene derivates, can improve the active layer morphology, recombination and extraction of charge carriers and, consequently, the FF.

[a] *Chongqing Institute of Green and Intelligent Technology, Chongqing School, University of Chinese Academy of Sciences (UCAS Chongqing), Chinese Academy of Sciences, Chongqing, 400714, China. E-mail: kanzhipeng@cigit.ac.cn, xiao.z@cigit.ac.cn, lushirong@cigit.ac.cn*

[b] *Zernike Institute for Advanced Materials, University of Groningen, Nijenborgh 4, NL-9747AG Groningen, The Netherlands*

[c] *Department of Energy & Materials Engineering, Dongguk University, Seoul, 100-715, Republic of Korea*

[d] *Department of Chemistry and Hong Kong Branch of Chinese National Engineering Research Center for Tissue Restoration & Reconstruction, Hong Kong University of Science and Technology (HKUST), Clear Water Bay, Kowloon, Hong Kong, China*

† Electronic supplementary information (ESI) available. See DOI: 10.1039/d0ee00714e

‡ Both authors contributed equally to this work.

Introduction

Organic solar cells (OSCs) have a promising application prospect in flexible and portable devices on account of their unique advantages, such as the tunable absorption range, the low material costs, the potential for large area device fabrications, and their lightweight.[1–7] Based on the types of electron donor and acceptor materials, OSCs can be categorized into all polymer OSCs, all small molecule (ASM) OSCs, and polymer/small

molecule OSCs. In comparison with their polymeric counterparts, small molecules have well-defined chemical structures, high purity of materials, and outstanding repeatability from batch to batch synthesis, making them more suitable for production on an industrial scale with printing techniques.[8–10] With the emergence of fused ring electron acceptors (FREAs), ASM OSCs with power conversion efficiency (PCE) above 13% were reported by selecting **Y6** as the electron acceptor.[11–16] However, small molecules tend to aggregate and form large domains, leading to serious donor/acceptor phase segregation.[17,18] As a result, ASM OSCs still lack device performance compared to OSCs with polymer donors and FREAs that show PCEs exceeding 17% in both single junction and in tandem structures.[19,20]

Considering the advantages of small molecules, it is clearly necessary to improve the photovoltaic performance of ASM OSCs. The PCE is a product of the open circuit voltage (V_{OC}), the short circuit current density (J_{SC}), and the fill factor (FF), so one or more subpar parameters can seriously limit the PCE. The V_{OC} and the J_{SC} can be potentially improved from designs of the energetic levels and the absorption ranges of the small molecule donor/acceptor,[9,21,22] while the FF cannot be predicted without the fabrication of the devices. However, higher FF can be obtained by optimization of the thin film morphologies, and approaches as solvent additives, solvent vapor annealing, and thermal annealing[11,17,23] have been proven to be effective methods to improve the FF of ASM OSCs. For instance, FF as high as 77% was obtained in BTR/**$PC_{71}BM$** based devices with solvent vapor treatment.[24] In contrast, the FFs of the optimized ASM OSCs based on FREAs were still lower than those of their fullerene counterparts. In particular, when **Y6** was selected as the electron acceptor, a PCE beyond 13% was gained by optimizing the active layer with thermal annealing prior to electrode deposition, but the FFs were lower than those of the OSCs with polymer donors.[9,17,21,25] For example, when **BTR-Cl** was blended with **Y6** as the active layer, the best FF was about 69%, which was *ca.* 10% lower than that of the devices made of PM6/**Y6**.[26] On the other hand, in high performance OSC systems geminate recombination is negligible, and bimolecular recombination becomes the major limiting factor of FF, which is predominantly determined by the recombination and charge extraction.[27] Accordingly, to further improve the FFs of ASM OSCs based on **Y6**, alternative morphology control methods and the charge carrier dynamic processes in the devices must be considered. Miscibility-induced morphology optimization is another recently-developed promising method to improve the thin film nanostructures by guest component incorporations.[28,29] It is demonstrated that incorporating more miscible materials in the active layer assists suppressed bimolecular recombination toward moderately improved FFs in OSCs with polymer donors.[30,31] Therefore, the regulation of a miscibility-induced microstructure to reduce charge recombination in the active layer can potentially enhance the FF and consequently the PCE.[27,32] Nevertheless, this practice is rarely applied in ASM OSCs, especially the incorporations of fullerenes as additives. Hence, to improve the performance of ASM OSCs composed of **BTR-Cl**/**Y6** that is limited by the FF, miscibility induced active layer optimization was adopted and fullerenes were chosen as the additives owing to their good miscibility with both **BTR-Cl** and **Y6**. In addition, although fullerenes as the third component were proved as a profitable method to improve J_{SC} and FF through the contribution of light absorption and morphology optimization,[33–36] there are few reports on applying fullerene as an additive to adjust the miscibility between the small molecular donor and acceptor.

In this contribution, we focus on the FF improvement of devices with **BTR-Cl**/**Y6** as the active layer, and **$PC_{71}BM$** was selected as the additive to rationally tune the active layer microstructures. The best performance was yielded when the **$PC_{71}BM$** loading was at *ca.* 5 wt% (**BTR-Cl : Y6 : $PC_{71}BM$**, 1.8 : 1 : 0.10, in wt%). We found that in comparison with the control devices, the optimized devices showed comparable charge extraction, longer charge carrier lifetime, and additionally, much lower bimolecular recombination rate (1.7×10^{-12} cm^3 s^{-1} *vs.* 9.0×10^{-12} cm^3 s^{-1}). Therefore, the optimized FF is improved from 69.63% to 77.11% (11.2% enhancement) with V_{OC} and J_{SC} maintained, leading to higher PCE of 15.34%. Moreover, we found that fullerene derivatives such as **$PC_{71}BM$**-C and $PC_{61}BM$ can also effectively improve the device performance. To the best of our knowledge, the PCE of 15.34% (certified at 14.7%, detail in Fig. S1, ESI†) is to date the highest efficiency for ASM OSCs.

Results and discussion

The chemical structures of the materials used in the active layers are presented in Fig. 1a. The energy levels of each material used in the active layer measured by cyclic voltammetry (CV) are shown in Fig. 1b, which are consistent with previous report.[12] The normalized absorbance spectra of the neat and the blend films are displayed in Fig. 1c and d, respectively. As observed from the absorbance of the blend films, the optimized one shows slightly enhanced absorption compared to that of the control one in the range of 300–450 nm due to the addition of **$PC_{71}BM$**. Besides, **$PC_{71}BM$** shows better miscibility with both **BTR-Cl** and **Y6** than the miscibility of **BTR-Cl**/**Y6**, which will be characterized and discussed in the morphology part.

Devices with architecture of ITO (indium tin oxide)/PEDOT:PSS/active layer (AL)/Phe-NaDPO/Ag were fabricated to evaluate the photovoltaic performance with the presence of **$PC_{71}BM$** in the active layer. Device performances with other fullerene derivatives are detailed in the ESI† (Fig. S2 and Table S1). The current density–voltage (*J*–*V*) is plotted in Fig. 1e and the detailed photovoltaic parameters are summarized in Table 1. As demonstrated,[13] the control device (active layer: **BTR-Cl**:**Y6**) exhibited a V_{OC} of 833.4 mV, a J_{SC} of 23.79 mA cm^{-2}, and an FF of 69.63%, resulting in a PCE of 13.81%. The optimized $PC_{71}CM$ loading was found at *ca.* 5 wt%, and the optimized devices (active layer: **BTR-Cl : Y6 : $PC_{71}BM$**, 1.8 : 1 : 0.1, in *ca.* 5 wt%) yield a V_{OC} of 837.8 mV, a J_{SC} of 23.75 mA cm^{-2}, and a boosted FF of 77.11%, leading to an outstanding PCE of 15.34%. The difference in PCE is visualized in the statistical chart (Fig. 1g). It is worth noting that the V_{OC} and J_{SC} of the optimized device were the same compared with those of the control devices. In particular, the identical V_{OC} implies that the

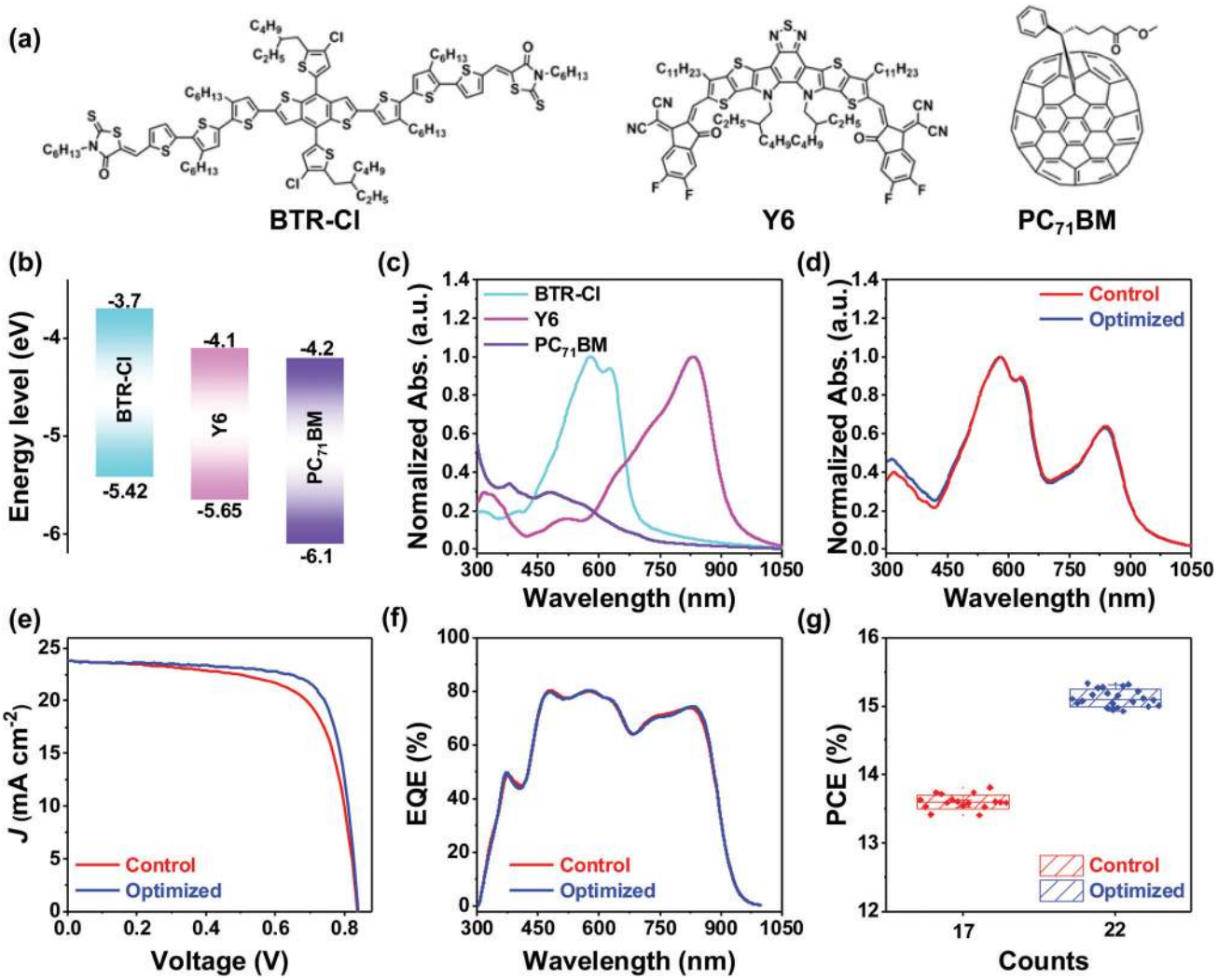

Fig. 1 Properties of materials and devices. (a) Chemical structures of **BTR-Cl**, **Y6** and **$PC_{71}BM$**; (b) energy levels of **BTR-Cl**, **Y6** and **$PC_{71}BM$**; (c) normalized absorbance spectra of **BTR-Cl**, **Y6** and **$PC_{71}BM$** in neat films; (d) normalized absorbance spectra of blend films w/o and with **$PC_{71}BM$**; (e) current density–voltage (*J*–*V*) curves of the control and optimized devices; (f) external quantum efficiency (EQE) of the control and optimized devices; and (g) the PCE distribution of the control and optimized devices.

Table 1 Summary of photovoltaic performance of the control and optimized devices

Device condition	V_{OC} (mV)	J_{SC} (mA cm^{-2})	FF (%)	PCE_{max}/PCE_{Ave}[a] (%)	J_{SC}[b] (mA cm^{-2})
Control	833.4	23.79	69.63	13.81/13.69	23.71
Optimized	837.8	23.75	77.11	15.34/15.14	23.65

[a] Statistical data obtained from 15 devices. [b] The J_{SC} calculated from the external quantum efficiency (EQE) curve.

addition of fullerene in the active layer is not significantly changing the energetic landscape, which is evidenced from the device optimizations with varied fullerene contents presented in Table S2 (ESI†); the J_{SC} was estimated by optical modeling[36] with refractive index and extinction coefficient from ellipsometry measurements, and it is noted that when the internal quantum efficiency was assumed to be 100%, the J_{SC} of devices w/o and with **$PC_{71}BM$** are the same as well (Fig. S2 and S3, ESI†). Therefore, the palpable enhancement of the efficiency is mainly attributed to the FF that increased from 69.63% to 77.11% in the optimized device. On the other hand, by close examination of the EQE spectra of the control and optimized devices, it is found that the EQE curves were identical as depicted in Fig. 1f. The superimposed EQE spectra suggest that the bandgaps and the integrated current density which directly estimate the V_{OC} and J_{SC} are the same. Thus, the **$PC_{71}BM$** as the guest component only improved the FF without influencing the energetic landscape and the photon to electron response of the active layer. To understand the improvement, we decided to check the charge extraction and recombination that determines the FF as well as the thin film morphologies.

In the operation of photovoltaic devices, FF relies on the transportation, extraction, collection, and recombination behaviors of photo-generated charges, and can be quantified to the rate of charge recombination and extraction. The electron and hole

mobility were derived by fitting the dark current density with the space charge limited current (SCLC) model. To get the dark current density, the electron only and hole only devices with architectures of ITO/PEDOT:PSS/AL/MoO_3/Ag and ITO/ZnO/Phen-NaDPO/AL/Phen-NaDPO/Ag were fabricated for active layers w/o and with **$PC_{71}BM$**. The electron and hole mobility values are presented in Fig. 2a and b and Table S3 (ESI†). Specifically, the electron and hole mobility values for the active layers w/o **$PC_{71}BM$** are 9.13×10^{-4} cm^2 V^{-1} s^{-1} and 9.97×10^{-4} cm^2 V^{-1} s^{-1}; and these values for the active layer with **$PC_{71}BM$** are 9.32×10^{-4} cm^2 V^{-1} s^{-1} and 9.78×10^{-4} cm^2 V^{-1} s^{-1}. Notably, the slightly increased electron mobility and decreased hole mobility from the film with **$PC_{71}BM$** affords more balanced electron and hole mobility.

Transient measurements on devices with laser perturbation can measure the dynamics of free charges. When the device is held at short circuit, transient photocurrent (TPC) is measured and information on charge extraction from the device can be obtained. Meanwhile, transient photovoltage (TPV) measurements record the voltage decay of a device kept at open circuit and facts related to charge recombination can be gained.[37] In addition, it was demonstrated that TPV measurements can be used as a direct measure of charge recombination kinetics in OSCs at open circuit by correlating the voltage decay with the decay of the polaron signal measured in transient absorption experiments.[38] Therefore, we performed these measurements to investigate the charge extraction and recombination patterns of the control and optimized devices. Considering the same J_{SC} for both devices, the charge extracted from each device under the same laser perturbation are the same, so we more focused on the charge extraction time. As depicted in TPC (Fig. 2c), the charge extraction time of the control and optimized devices are 0.88 μs and 0.86 μs, indicating that the charge extraction from the control device is as efficient as that from the optimized device. In other words, charge extraction is not a factor that led to the improvement. Next, we examined the charge recombination *via* TPV measurement. The carrier lifetime (τ) was extracted from fitting of the TPV signal with equation: $y = A \times \exp(-x/t)$, and values of 0.84 μs and 1.95 μs were obtained for the control and optimized devices, respectively. The τ with values of 1.95 μs from the device with 5 wt% **$PC_{71}BM$** is *ca.* 2.3 times longer than that from the control device w/o **$PC_{71}BM$**, implying that charge recombination is greatly suppressed in the device with **$PC_{71}BM$** (optimized device). Meanwhile, the mono-exponential fit of the voltage decay suggests that only one recombination route exists in the devices.[39] Hence, the suppressed charge recombination upon the loading of **$PC_{71}BM$** is the major factor causing the improvement in FF. However, what kind of recombination is

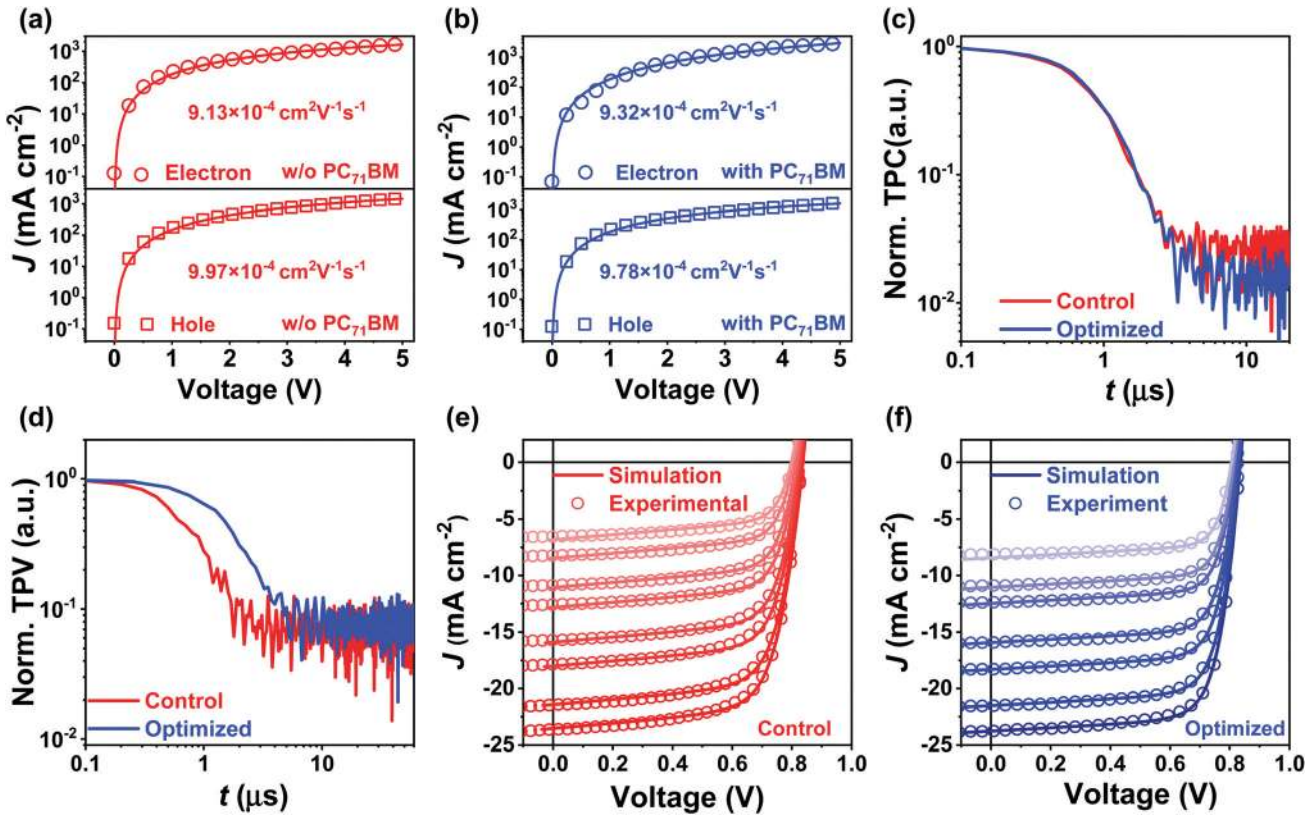

Fig. 2 Characteristics of charge carrier mobility, charge extraction and recombination, and drift diffusion simulations. (a) Dark current density of the electron and hole only devices w/o **$PC_{71}BM$** (the solid lines are fittings to the SCLC model); (b) dark current density of the electron and hole only devices with **$PC_{71}BM$** (the solid lines are fittings to the SCLC model); (c) transient photocurrent of the control and optimized devices; (d) transient photovoltage of the control and optimized devices; (e) *J*–*V* curves with various incident light intensities of the control devices (the solid lines are the fitting to the 1D drift diffusion model); and (f) *J*–*V* curves with various incident light intensities of the optimized devices (the solid lines are the fitting to the 1D drift diffusion model).

Table 2 Parameters of control and optimized devices *via* drift-diffusion simulations

Parameter	Symbol	Control device	Optimized device
Average generation rate (1 sun)	G	1.475×10^{28} m^{-3} s^{-1}	1.239×10^{28} m^{-3} s^{-1}
Effective density of states	N_c	4.9×10^{26} m^{-3}	1.55×10^{26} m^{-3}
HOMO (effective)	E_{HOMO}	−5.42	−5.42
LUMO (effective)	E_{LUMO}	−4.1	−4.2
Relative dielectric constant	ε_r	3.5	3.5
Electron mobility*	μ_n	9.13×10^{-8} m^2 V^{-1} s^{-1}*	9.32×10^{-8} m^2 V^{-1} s^{-1}*
Hole mobility*	μ_p	9.97×10^{-8} m^2 V^{-1} s^{-1}*	9.78×10^{-8} m^2 V^{-1} s^{-1}*
Bimolecular recombination rate	k_{BR}	9×10^{-18} m^3 s^{-1}	1.7×10^{-18} m^3 s^{-1}
Anode work function	W_R	−5.42 eV	−5.42 eV
Cathode work function	W_L	−4.2 eV	−4.2 eV
Shunt resistance	R_{shunt}	0.09 Ω m^{-2}	0.14 Ω m^{-2}
Series resistance	R_{series}	1.6×10^{-4} Ω m^{-2}	1.35×10^{-4} Ω m^{-2}

The parameters marked with "*" are the experimental data.

present in the device cannot be distinguished by performing only TPV measurements, and other characterizations are needed.

Simulations by means of drift-diffusion modeling take into account charge generation, recombination effects, and the carrier mobilities of the active layer by numerically solving the drift-diffusion equations that govern the *J–V* characteristics. To get the detailed information about the control and optimized devices, we performed 1 dimensional (1D) drift-diffusion modeling[40] of the *J–V* curves of ASM OSCs with various incident light intensities by using parameters such as energy levels, refractive index, extinction coefficient, and charge carrier mobility measured for the materials and devices. The simulated parameters are presented in Table 2. Notably, traps are absent in both the control and optimized devices, and the bimolecular recombination rates are quite different. The absence of significant trapping is in line with the TPV fittings that only one recombination route, *i.e.* bimolecular recombination, presents in the control and optimized devices. The recombination rate of a control device is 9×10^{-12} cm^3 s^{-1}, which is much higher than that of the optimized device with values of 1.7×10^{-12} cm^3 s^{-1}. Thus far, the charge extraction and recombination features are analyzed quantitatively. The optimized device has similar charge extraction conditions to the control device, but significantly reduced bimolecular recombination rate, leading to the enhancement of FF.

The altered electronic parameters in devices usually originate from the morphology changes in the device active layer; therefore, we decided to check the miscibility of the donor/acceptor materials, the surface/bulk morphology, and the crystalline features of the films to examine the potential contributions of morphological effects w/o and with **$PC_{71}BM$** to the distinct FF. The miscibility of two components in the blend can be estimated from the solubility parameters (δ) of each material. When the δ for two materials is comparable, *i.e.* the difference in the absolute value ($\Delta\delta$) is small enough, they are more miscible in the blend, indicating that two components will be finely mixed, and less phase separated in the blend.[41–45] The solubility parameters (δ) can be calculated with eqn (1),

$$\delta = K\sqrt{\gamma} \quad (1)$$

where γ is the surface energy of the material, and K is the proportionality constant ($K = 116 \times 10^3$ m$^{-1/2}$).[46–48] The surface energy of each material was calculated from the contact angle measurements (details in Fig. S5 and Table S4, ESI†), and the details are listed in Table 3. The δ values for **BTR-Cl**, **Y6**, and **$PC_{71}BM$** are 4.28 K, 5.79 K and 5.57 K, respectively, indicating that the miscibility of **$PC_{71}BM$/Y6** and **BTR-Cl/$PC_{71}BM$** is better than that of **BTR-Cl/Y6.** It is noteworthy to mention that though the miscibility of two materials can be characterized by the solubility parameters derived from the surface energy, the origin of the increased miscibility may result from the entropy of mixing.[49–51] Moreover, the absolute difference of δ is listed in Table 3 as well. These findings were also revealed from the microscopy measurements, showing reduced aggregation and fine mixed phases.

Table 3 Surface energy (γ), solubility parameters (δ), and the absolute difference of δ ($\Delta\delta$)

Film	γ (mN m^{-1})	$\delta \times K$	$\Delta\delta$ ($\times K$)
BTR-Cl	18.3	4.28	—
Y6	33.49	5.79	—
$PC_{71}BM$	31.04	5.67	—
BTR-Cl:Y6	—	—	2.28
BTR-Cl:$PC_{71}BM$	—	—	1.67
Y6:$PC_{71}BM$	—	—	0.046

The surface and bulk morphology of the thin films w/o and with **$PC_{71}BM$** were characterized by atomic force microscopy (AFM) and transmission electron microscopy (TEM), respectively. As demonstrated in Fig. 3a and b, the films show various extents of aggregation. In particular, the pronounced aggregation (RMS: 2.20 nm) observed in the film w/o **$PC_{71}BM$** contrasts with that for the film with **$PC_{71}BM$** (RMS: 2.88 nm). Usually, the surface roughness tells the crystallinity features beneath,[52] and the increased roughness may correlate with the increased crystallinity of the active layer. These features are observed in the TEM images (Fig. 3c and d) as well. The better mixed phases observed for the film with **$PC_{71}BM$** demonstrate that the miscibility introduced morphology leads to well-formed morphology and phase separation, benefiting the charge separation and transportation.

The crystalline features and nanoscale phase segregations of the thin films w/o and with **$PC_{71}BM$** were examined by grazing incident X-ray scattering. The molecular packing properties were measured by grazing incident wide angle X-ray scattering

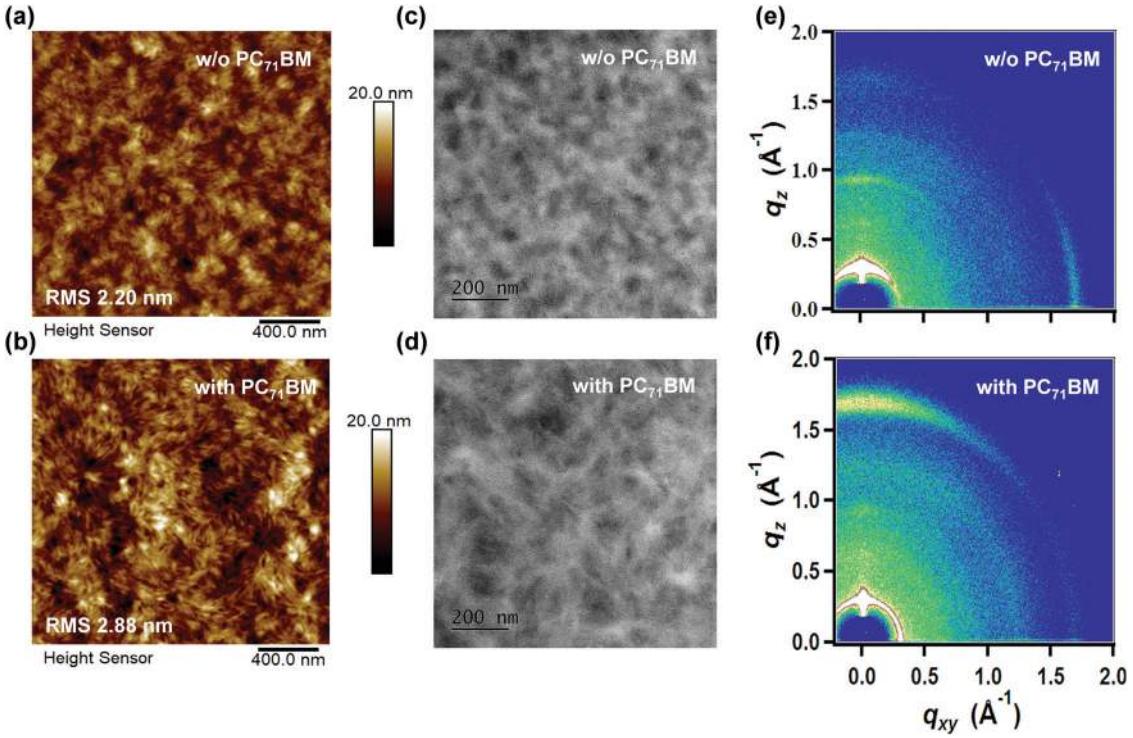

Fig. 3 Morphology characteristics. AFM images (2 × 2 μm) of (a) film w/o **$PC_{71}BM$**, and (b) film with **$PC_{71}BM$**; the scale bars are 400 nm. TEM images of (c) film w/o **$PC_{71}BM$**, and (d) film with **$PC_{71}BM$**. The scale bars are 200 nm. 2D GIWAXS patterns of (e) film w/o **$PC_{71}BM$**, and (f) film with **$PC_{71}BM$**.

(GIWAXS), and the 2D figures are shown in Fig. 3e and f, respectively. The 1D patterns including in-plane (IP) and out-of-plane (OOP) profiles of these films are presented in Fig. S7 (ESI†) and the parameters are summarized in Table S5 and S6 (ESI†). Two distinct features are observed from the GIWAXS results: first, both films exhibit a distinct (100) peak at q = 0.29 Å^{-1} and a (300) peak at q = 0.95 Å^{-1} in the OOP direction, and a (100) peak at q = 0.34 Å^{-1} and a (010) peak at q = 1.72 Å^{-1} in the IP direction; second, when *ca.* 5 wt% **$PC_{71}BM$** was present in the film, the molecular orientation was altered to preferential face-on direction, leading to a totally different charge hopping network compared with the films w/o **$PC_{71}BM$**. Therefore, the introduction of **$PC_{71}BM$** transformed the edge-on governed blend effectively to a face-on predominant morphology. On the one hand, **$PC_{71}BM$** is well-known as an electron transporting isotropic material, which is favorable for electron transport in any direction.[53] In addition, **BTR-Cl** presents a typical edge-on orientation and **Y6** displays a representative face-on orientation.[12,54] As a result, the transformation not only constructs a novel pathway for carrier hopping, but also optimizes the morphology with suppressed **BTR-Cl** phase yet pronounced **Y6** phase, which is in good agreement with the changes in the hole and electron mobilities.

Subsequent to the crystallinity characterizations, the nanoscale structural information of the active layers was monitored by grazing incident small angle X-ray scattering (GISAXS) measurements (Fig. S8, ESI†). The estimated pure phase domain size of the film w/o and with **$PC_{71}BM$** are 31.8 nm and 23.9 nm, respectively. In comparison, the domain size of the film with $P_{71}CM$ is closer to the theoretical exciton diffusion length,[55,56] which can be beneficial for the exciton dissociations and charge separations. The changes in the molecular orientation and the pure phase domain size further confirm that the miscibility-induced microstructures driven by the more miscible **$PC_{71}BM$** is the key to delicately manipulating the morphology to achieve significantly suppressed charge recombination and thus improved FF towards high-performing all-small-molecule photovoltaics.

Conclusions

In summary, ASM OSCs composed of **BTR-Cl** and **Y6** as the active layer with **$PC_{71}BM$** as additive were fabricated and characterized. Compared to the control devices, the optimized devices with *ca.* 5 wt% **$PC_{71}BM$** in the active layer yielded a higher FF of 77.11% with identical V_{OC} and J_{SC}, resulting in a record PCE of 15.34% (certified at 14.7%). Based on the findings from measurements of TPC and TPV, and the drift-diffusion simulations, the origin of the FF improvement was attributed to the significantly reduced bimolecular recombination caused by the introduction of the **$PC_{71}BM$**. With additional morphology characterization, we found that when more miscible fullerene derivatives were incorporated as the guest component in the active layer, the donor/acceptor phase is better mixed with the formation of more reasonable domain size, and the edge-on oriented crystalline phases changed to face-on orientations, forming favorable microstructures for charge separation and transportations in the vertical direction in devices. The approach

presented here paves the way to a deeper understanding of the miscibility-induced morphology regulations and the FF improvement resulting from the incorporation of more miscible materials and provides direct guidelines for optimization of the active layers in ASM OSCs.

Conflicts of interest

The authors declare no conflict of interest.

Acknowledgements

S. L. thanks the research grant from the National Youth Thousand Program Project (R52A199Z11) and the "artificial intelligence" key project of Chongqing (No. cstc2017rgzn-zdyfX0030). Z. K. acknowledges the research grants from CAS Pioneer Hundred Talents Program (Y82A060Q10, Y92A160Q10, E0296102), and the National Natural Science Foundation of China (no. 61805245); Z. X. thanks the research support from CAS Pioneer Hundred Talents Program B (Y92A010Q10), the National Natural Science Foundation of China (21801238), and the Natural Science Foundation of Chongqing (cstc2018jcyjAX0556), Venture & Innovation Support Program for Chongqing Overseas Returnees (cx2019028), Chongqing Talents Top Youth Talent Program (CQYC201905057). H. C. thanks the research grants from the Natural Science Foundation of Chongqing (cstc2019jcyj-msxmX0400). V. M. L. C. is supported by a grant from STW/NWO (VIDI 13476). The authors thank Huirong Su from Genuine Optronics Ltd for the measurements of ellipsometry and data analysis. The authors thank Dr Manish Kumar for the measurements of GIWAXS at Pohang Accelerator Laboratory. H. C. thanks the research grant from the project of Youth Innovation Promotion Association, Chinese Academy of Sciences.

References

1 Q. An, F. Zhang, J. Zhang, W. Tang, Z. Deng and B. Hu, *Energy Environ. Sci.*, 2016, **9**, 281–322.
2 L. Yang, S. Zhang, C. He, J. Zhang, H. Yao, Y. Yang, Y. Zhang, W. Zhao and J. Hou, *J. Am. Chem. Soc.*, 2017, **139**, 1958–1966.
3 X. Meng, L. Zhang, Y. Xie, X. Hu, Z. Xing, Z. Huang, C. Liu, L. Tan, W. Zhou, Y. Sun, W. Ma and Y. Chen, *Adv. Mater.*, 2019, **31**, 1903649.
4 Z. Luo, R. Sun, C. Zhong, T. Liu, G. Zhang, Y. Zou, X. Jiao, J. Min and C. Yang, *Sci. China: Chem.*, 2020, **63**, 361–369.
5 R. Ma, T. Liu, Z. Luo, Q. Guo, Y. Xiao, Y. Chen, X. Li, S. Luo, X. Lu, M. Zhang and H. Yan, *Sci. China: Chem.*, 2020, **63**, 325–330.
6 T. Liu, Z. H. Luo, Q. P. Fan, G. Y. Zhang, L. Zhang, W. Gao, X. Guo, W. Ma, M. J. Zhang, C. L. Yang, Y. F. Li and H. Yan, *Energy Environ. Sci.*, 2018, **11**, 3275–3282.
7 K. Gao, S. B. Jo, X. Shi, L. Nian, M. Zhang, Y. Kan, F. Lin, B. Kan, B. Xu, Q. Rong, L. Shui, F. Liu, X. Peng, G. Zhou, Y. Cao and A. K. Y. Jen, *Adv. Mater.*, 2019, **31**, 1807842.
8 Y. Z. Lin, Y. F. Li and X. W. Zhan, *Chem. Soc. Rev.*, 2012, **41**, 4245–4272.
9 Y. Wang, Y. Wang, B. Kan, X. Ke, X. Wan, C. Li and Y. Chen, *Adv. Energy Mater.*, 2018, **8**, 1802021.
10 B. Qiu, L. Xue, Y. Yang, H. Bin, Y. Zhang, C. Zhang, M. Xiao, K. Park, W. Morrison, Z. Zhang and Y. Li, *Chem. Mater.*, 2017, **29**, 7543–7553.
11 Q. Yue, H. Wu, Z. Zhou, M. Zhang, F. Liu and X. Zhu, *Adv. Mater.*, 2019, **31**, 1904283.
12 H. Chen, D. Hu, Q. Yang, J. Gao, J. Fu, K. Yang, H. He, S. Chen, Z. Kan, T. Duan, C. Yang, J. Ouyang, Z. Xiao, K. Sun and S. Lu, *Joule*, 2019, **3**, 3034–3047.
13 R. Zhou, Z. Jiang, C. Yang, J. Yu, J. Feng, M. A. Adil, D. Deng, W. Zou, J. Zhang, K. Lu, W. Ma, F. Gao and Z. Wei, *Nat. Commun.*, 2019, **10**, 5393.
14 J. F. Ge, L. C. Xie, R. X. Peng, B. Fanady, J. M. Huang, W. Song, T. T. Yan, W. X. Zhang and Z. Y. Ge, *Angew. Chem., Int. Ed.*, 2020, **59**, 2808–2815.
15 C. Q. Yan, S. Barlow, Z. H. Wang, H. Yan, A. K.-Y. Jen, S. R. Marder and X. W. Zhan, *Nat. Rev. Mater.*, 2018, **3**, 18003.
16 Y. Z. Lin, J. Y. Wang, Z. G. Zhang, H. T. Bai, Y. F. Li, D. B. Zhu and X. W. Zhan, *Adv. Mater.*, 2015, **27**, 1170–1174.
17 Y. Huo, X. Gong, T. Lau, T. Xiao, C. Yan, X. Lu, G. Lu, X. Zhan and H. Zhang, *Chem. Mater.*, 2018, **30**, 8661–8668.
18 H. Wu, H. J. Fan, W. Y. Liu, S. S. Chen, C. D. Yang, L. Ye, H. Ade and X. Z. Zhu, *Small*, 2019, **15**, 1902656.
19 L. Meng, Y. Zhang, X. Wan, C. Li, X. Zhang, Y. Wang, X. Ke, Z. Xiao, L. Ding, R. Xia, H. Yip, Y. Cao and Y. Chen, *Science*, 2018, **361**, 1094–1098.
20 H. Bin, J. Yao, Y. Yang, I. Angunawela, C. Sun, L. Gao, L. Ye, B. Qiu, L. Xue, C. Zhu, C. Yang, Z. Zhang, H. Ade and Y. Li, *Adv. Mater.*, 2018, **30**, 1706361.
21 Y. Wang, Y. Wang, B. Kan, X. Ke, X. Wan, C. Li and Y. Chen, *Adv. Energy Mater.*, 2018, **8**, 1802021.
22 T. Liu, Z. H. Luo, Y. Z. Chen, T. Yang, Yi. Q. Xiao, G. Y. Zhang, R. J. Ma, X. H. Lu, C. L. Zhan, M. J. Zhang, C. L. Yang, Y. F. Li, J. N. Yao and H. Yan, *Energy Environ. Sci.*, 2019, **12**, 2529–2536.
23 Y. Huo, H. L. Zhang and X. W. Zhan, *ACS Energy Lett.*, 2019, **4**, 1241–1250.
24 K. Sun, Z. Xiao, S. Lu, W. Zajaczkowski, W. Pisula, E. Hanssen, J. M. White, R. M. Williamson, J. Subbiah, J. Ouyang, A. B. Holmes, W. W. H. Wong and D. J. Jones, *Nat. Commun.*, 2015, **6**, 6013.
25 H. Tang, T. L. Xu, C. Q. Yan, J. Gao, H. Yin, J. Lv, R. Singh, M. Kumar, T. N. Duan, Z. P. Kan, S. R. Lu and G. Li, *Adv. Sci.*, 2019, **6**, 1901613.
26 L. Liu, Y. Y. Kan, K. Gao, J. X. Wang, M. Zhao, H. Chen, C. J. Zhao, T. G. Jiu, A. K. Y. Jen and Y. L. Li, *Adv. Mater.*, 2020, **32**, 1907604.
27 D. Bartesaghi, I. D. C. Pérez, J. Kniepert, S. Roland, M. Turbiez, D. Neher and L. J. A. Koster, *Nat. Commun.*, 2015, **6**, 8083.
28 J. Lv, Y. Feng, J. Fu, J. Gao, R. Singh, M. Kumar, M. Kim, H. Tang, S. Lu, W. Zhang, I. McCulloch, J. Li and Z. Kan, *Sol. RRL*, 2019, **4**, 1900403.

29 H. B. Naveed and W. Ma, *Joule*, 2018, **2**, 621–641.
30 D. Baran, R. S. Ashraf, D. A. Hanifi, M. Abdelsamie, N. Gasparini, J. A. Röhr, S. Holliday, A. Wadsworth, S. Lockett, M. Neophytou, C. J. M. Emmott, J. Nelson, C. J. Brabec, A. Amassian, A. Salleo, T. Kirchartz, J. R. Durrant and I. McCulloch, *Nat. Mater.*, 2017, **16**, 363–369.
31 S. Albrecht, W. Schindler, J. Kurpiers, J. Kniepert, J. C. Blakesley, I. Dumsch, S. Allard, K. Fostiropoulos, U. Scherf and D. Neher, *J. Phys. Chem. Lett.*, 2012, **3**, 640–645.
32 G. F. Burkhard, E. T. Hoke and M. D. McGehee, *Adv. Mater.*, 2010, **22**, 3293–3297.
33 T. Yan, W. Song, J. Huang, R. Peng, L. Huang and Z. Ge, *Adv. Mater.*, 2019, **31**, 1902210.
34 M. A. Pan, T.-K. Lau, Y. Tang, Y. C. Wu, T. Liu, K. Li, M. C. Chen, X. Lu, W. Ma and C. Zhan, *J. Mater. Chem. A*, 2019, **7**, 20713–20722.
35 C. Xu, J. Wang, Q. An, X. Ma, Z. Hu, J. Gao, J. Zhang and F. Zhang, *Nano Energy*, 2019, **66**, 104119.
36 L. L. Zhan, S. Li, T. K. Lau, Y. Cui, X. Lu, M. Shi, C. Li, H. Li, J. Hou and H. Chen, *Energy Environ. Sci.*, 2020, **13**, 635.
37 Z. Li, F. Gao, N. C. Greenham and C. R. McNeill, *Adv. Funct. Mater.*, 2011, **21**, 1419–1431.
38 C. G. Shuttle, B. O. Regan, A. M. Ballantyne, J. Nelson, D. D. C. Bradley, J. de Mello and J. R. Durrant, *Appl. Phys. Lett.*, 2008, **92**, 93311.
39 Z. Li, F. Gao, N. C. Greenham and C. R. McNeill, *Adv. Funct. Mater.*, 2011, **21**, 1419–1431.
40 L. Koster, E. Smits, V. Mihailetchi and P. Blom, *Phys. Rev. B: Condens. Matter Mater. Phys.*, 2005, **72**, 085205.
41 S. Pang, R. Zhang, C. Duan, S. Zhang, X. Gu, X. Liu, F. Huang and Y. Cao, *Adv. Energy Mater.*, 2019, **9**, 1901740.
42 K. Kim, H. Kang, H. J. Kim, P. S. Kim, S. C. Yoon and B. J. Kim, *Chem. Mater.*, 2012, **24**, 2373–2381.
43 L. Ye, B. A. Collins, X. Jiao, J. Zhao, H. Yan and H. Ade, *Adv. Energy Mater.*, 2018, **8**, 1703058.
44 X. Liu, C. Zhang, C. Duan, M. Li, Z. Hu, J. Wang, F. Liu, N. Li, C. J. Brabec, R. Janssen, G. C. Bazan, F. Huang and Y. Cao, *J. Am. Chem. Soc.*, 2018, **140**, 8934–8943.
45 L. Ye, H. Hu, M. Ghasemi, T. Wang, B. A. Collins, J. Kim, K. Jiang, J. H. Carpenter, H. Li, Z. Li, T. McAfee, J. Zhao, X. Chen, J. L. Y. Lai, T. Ma, J. Bredas, H. Yan and H. Ade, *Nat. Mater.*, 2018, **17**, 253–260.
46 S. Nilsson, A. Bernasik, A. Budkowski and E. Moons, *Macromolecules*, 2007, **40**, 8291–8301.
47 S. Kouijzer, J. J. Michels, M. van den Berg, V. S. Gevaerts, M. Turbiez, M. M. Wienk and R. A. J. Janssen, *J. Am. Chem. Soc.*, 2013, **135**, 12057–12067.
48 H. Wu, H. J. Fan, S. J. Xu, L. Ye, Y. Guo, Y. P. Yi, H. Ade and X. Z. Zhu, *Small*, 2019, **15**, 1804271.
49 A. D. Z. Mendaza, A. Melianas, S. Rossbauer, O. Bäcke, L. Nordstierna, P. Erhart, E. Olsson, T. D. Anthopoulos, O. Inganäs and C. Müller, *Adv. Mater.*, 2015, **27**, 7325–7331.
50 J. J. Richards, A. H. Rice, R. D. Nelson, F. S. Kim, S. A. Jenekhe, C. K. Luscombe and D. C. Pozzo, *Adv. Funct. Mater.*, 2013, **23**, 514–522.
51 A. D. Z. Mendaza and C. Müller, *Adv. Energy Mater.*, 2018, **8**, 1702741.
52 Y. H. Liu, J. B. Zhao, Z. K. Li, C. Mu, W. Ma, H. W. Hu, K. Jiang, H. Lin, H. Ade and H. Yan, *Nat. Commun.*, 2014, **5**, 5293.
53 J. Huang, C. Z. Li, C. C. Chueh, S. Q. Liu, J. S. Yu and A. K. Y. Jen, *Adv. Energy Mater.*, 2015, **5**, 1500406.
54 J. Yuan, Y. Z. Zhang, L. Y. Zhou, G. C. Zhang, H. L. Yip, T.-K. Lau, X. H. Lu, C. Zhu, H. J. Peng, P. A. Johnson, M. Leclerc, Y. Cao, J. Ulanski, Y. F. Li and Y. P. Zou, *Joule*, 2018, **3**, 1140–1151.
55 O. V. Mikhnenko, P. W. M. Blom and T. Q. Nguyen, *Energy Environ. Sci.*, 2015, **8**, 1867–1888.
56 F. Liu, Y. Gu, C. Wang, W. Zhao, D. Chen, A. L. Briseno and T. P. Russell, *Adv. Mater.*, 2012, **24**, 3947–3951.